NANO LETTERS

pubs.acs.org/NanoLett

Letter

Femtosecond Laser Fabrication of Three-Dimensional Bubble-Propelled Microrotors for Multicomponent Mechanical Transmission

Dawei Wang, Chen Xin,* Liang Yang, Liu Wang, Bingrui Liu, Hao Wu, Chaowei Wang, Deng Pan, Zhongguo Ren, Yanlei Hu, Jiawen Li, Jiaru Chu, and Dong Wu*

Cite This: https://doi.org/10.1021/acs.nanolett.4c00037

Read Online

ACCESS | Metrics & More | Article Recommendations | Supporting Information

ABSTRACT: Inspired by the reverse thrust generated by fuel injection, micromachines that are self-propelled by bubble ejection are developed, such as microrods, microtubes, and microspheres. However, controlling bubble ejection sites to build micromachines with programmable actuation and further enabling mechanical transmission remain challenging. Here, bubble-propelled mechanical microsystems are constructed by proposing a multimaterial femtosecond laser processing method, consisting of direct laser writing and selective laser metal reduction. The polymer frame of the microsystems is first printed, followed by the deposition of catalytic platinum into the desired local site of the microsystems by laser reduction. With this method, a variety of designable microrotors with selective bubble ejection sites are realized, which enable excellent mechanical transmission systems composed of single and multiple mechanical components, including a coupler, a crank slider, and a crank rocker system. We believe the presented bubble-propelled mechanical microsystems could be extended to applications in microrobotics, microfluidics, and microsensors.

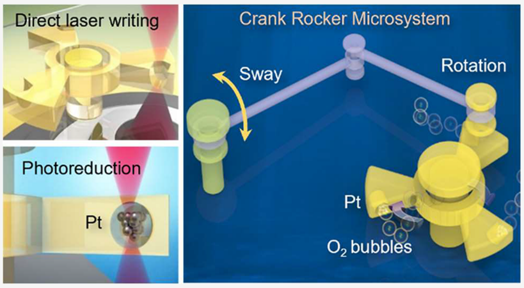

KEYWORDS: *microrotor, femtosecond laser, direct laser writing, photoreduction, micromachines*

Recently, micromachines that can convert energy into mechanical motion have attracted a great deal of interest.[1,2] In a typical micromachine system, the microrotor is a crucial component acting as a power source, continuously rotating to provide torque to other microdevices.[3] At the microscale, propulsion of the microrotor is usually achieved by applying external magnetic,[4,5] electrical,[6,7] optical,[8−10] or ultrasonic fields[11−13] throughout the workspace, which leads to low selectivity or high complexity in the design and fabrication of the micromechanical systems.[14,15] In addition, the continued presence of the external fields also requires substantial energy input.[16,17] Thus, a simple driving mode to complete the individual control of microrotors and further move the power to the entire microsystems is urgently needed.

As an independent and self-propelled mode, microtubes and microspheres powered by the bubble ejection mode have attracted a great deal of attention because of their large propulsion power and robustness in performing a variety of tasks.[18−20] Bubble ejections are usually produced by the catalyst-assisted chemical reaction between solution and active or noble metals,[21] such as silver (Ag), magnesium (Mg), zinc (Zn), and platinum (Pt). To endow the micromotor with strong thrust and controllable locomotion, the location of the catalyst used to control the bubble ejection sites is of the essence. Current catalyst deposition methods usually rely on surface deposition techniques[22] or template electrodeposition technology.[23] For example, the Mg layer is usually covered on the exposed surface of microparticles by physical deposition to form Janus microspheres.[24,25] Similarly, the Pt layer is deposited to the inner surface of a tube by electrodeposition to build bubble-propelled microtubes.[26] However, the catalytic materials are indiscriminately deposited on the whole exposed surface by the methods mentioned above, making it difficult to cover heterotypic structures or more complex structures with curved inner cavities.[27] Although there have been some reports of selective deposition of Pt, such as using mask layer exposure methods[28] or using laser scanning of treated surfaces,[29] these methods are unable to achieve deposition in the inner surface of the microstructure or require complex chemical processes that only work on treated material surfaces. In addition, bubble-propelled multicomponent mechanical systems and their transmission functions remain unrealized. The primary reasons are twofold. First, current processing strategies, including chemical synthesis and template deposition, have weak three-dimensional structure fabrication capabilities and low processing accuracy, making it difficult to construct micromechanical systems that require the precise assembly of

Received: January 3, 2024
Revised: February 25, 2024
Accepted: February 27, 2024

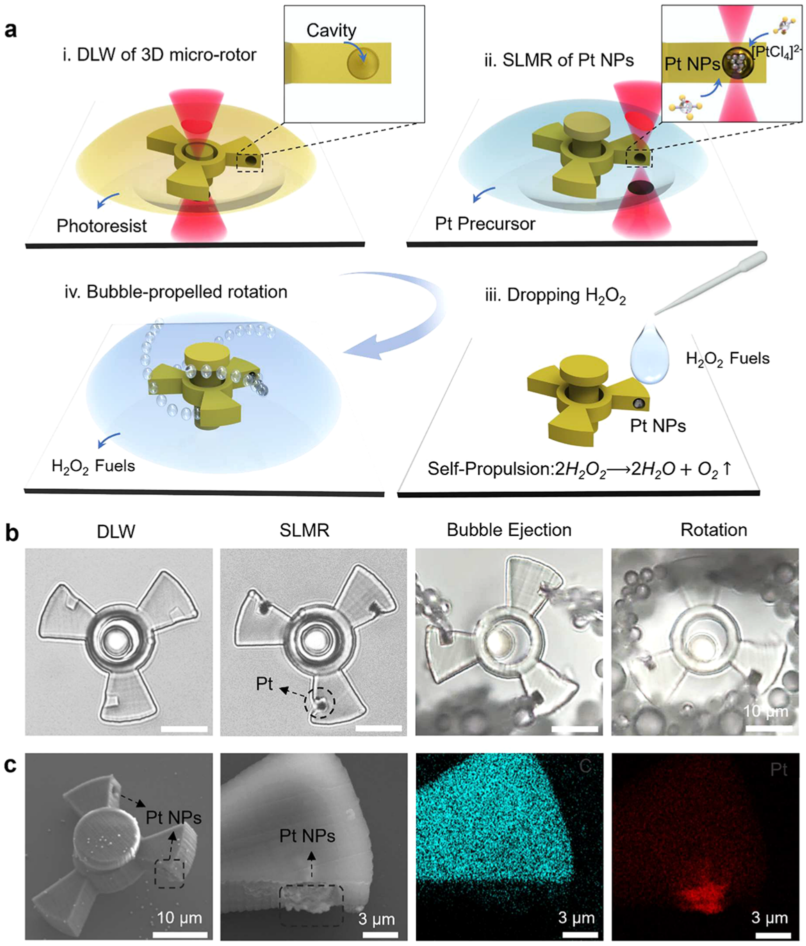

Figure 1. Fabrication of self-propelled microrotors with a selective bubble ejection site. (a) Schematic illustration of DLW combined with the SLMR method to fabricate a microrotor. (i) Skeleton of microrotors prepared by femtosecond laser direct writing in photoresist SZ2080. The inset denotes the blade with a cavity is fabricated by DLW. (ii) Site-selective photoreduction of catalytic platinum. The inset depicts Pt nanoparticles (NPs) generated after the process of SLMR in the hollow cavity of the microrotor skeleton. (iii) After a two-step fabrication process, the sample is rinsed and H_2O_2 is dropped for the next actuation. (iv) As-prepared microrotor rotation in the hydrogen peroxide solution. (b) Optical microscopy images of the skeleton and fabrication process of the microrotor. The hollow cavity of the microrotor on the left image can be seen distinctly, which is favors the subsequent photoreduction process. The second image is the optical microscopy image of an as-prepared microrotor selectively deposited catalytic Pt nanoparticle cluster in each blade. Optical microscopy of the third and fourth images illustrates the ejection of bubbles from each static blade until rotating in a short time. (c) SEM image of the prepared microrotor skeleton (in a side 45° view) (left). The second to fourth images are corresponding EDS spectroscopy images illustrating the platinum nanoparticles are loaded into the cavity of the blades.

multiple components. Furthermore, due to the lack of precise positioning of catalytic materials into three-dimensional (3D) space by current methods, the sites and quantity of bubble propulsion sources are difficult to precisely control in micromechanical systems.

Herein, we propose a simple strategy for fabricating micromechanical systems with complex geometry and controllable bubble ejection sites, consisting of direct laser writing (DLW) and selective laser metal reduction (SLMR). In the first step, a microrotor with a cavity in each side wall is fabricated by DLW. In the second step, the selected cavities of the microrotor are specifically deposited with catalytic metal nanoparticles by SLMR. Via the selective control of the catalyst deposition site, the rotation speed of the microrotors could be flexibly controlled. Compared with other existing rotors, self-propelled microrotors demonstrate an independent rotation direction and high robustness in opaque media and dark environments. Furthermore, as a self-propelled power source, the microrotors are integrated into various multicomponent mechanical transmission systems, such as microcoupling, a crank slider, and a crank rocker. We believe these mechanical transmission systems have potential applications in microrobotics,[30] microparticle manipulation,[31] and microfluidics.

Fabrication of Self-Propelled Microrotors with Selective Bubble Ejection Sites. Designable 3D structures and selectable bubble ejection sites are two key factors in achieving programmable rotation of self-propelled microrotors. Specifically, femtosecond laser processing enables both DLW of true 3D microrotor skeletons and SLMR of catalytic metal nanoparticles in localized regions of the skeleton.[32−34] Here, we combine femtosecond laser photopolymerization and photoreduction to enable microrotors with selective bubble ejection sites. The first step is to print the microrotor skeleton by femtosecond laser two-photon polymerization [Figure 1a(i)]. The morphology of the skeleton microrotor is further characterized by the optical profilometer (Figure S1, Note S1, and Experimental Section). Subsequently, the second step called SLMR is applied to deposit Pt into the desired site [Figure 1a(ii), Movie S1, and Experimental Section]. When the femtosecond laser beam is focused into the reserved cavity

https://doi.org/10.1021/acs.nanolett.4c00037

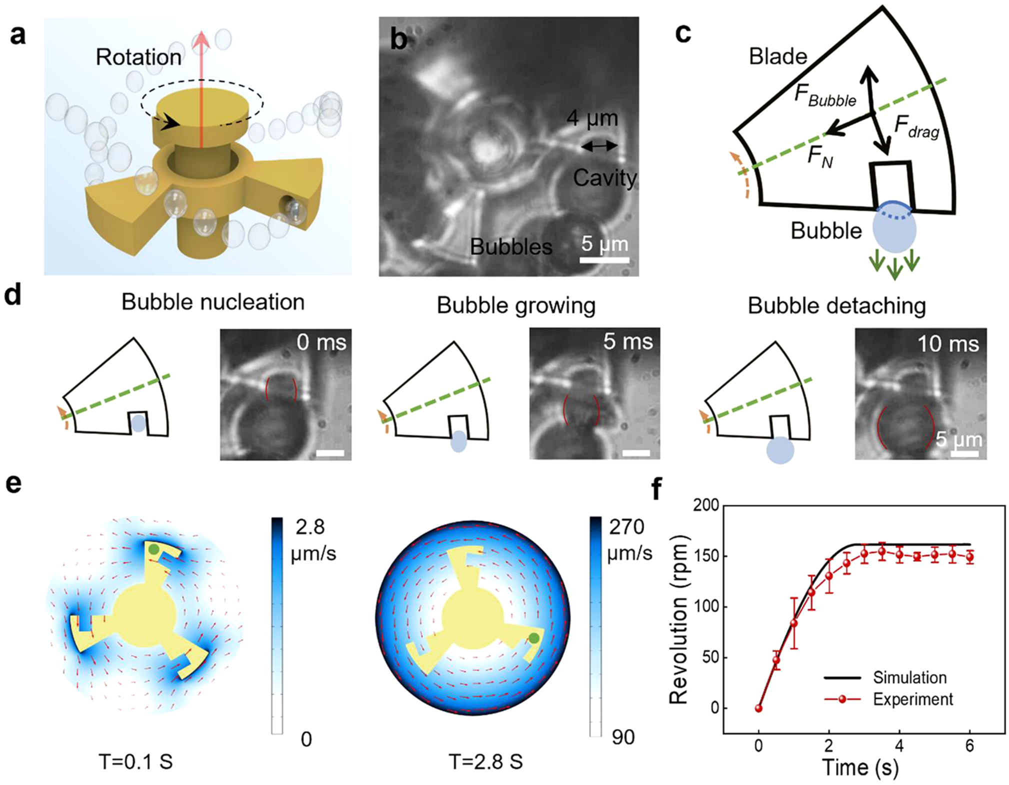

Figure 2. Kinematic simulation of a microrotor. (a) Schematic of the rotation of a microrotor based on bubble ejection. (b) Frame of the rotation under the high-speed camera showing the process of bubble ejection. (c) Force analysis diagram of the rotating microrotor denoting the microrotor is subject to three main forces during rotation. (d) Growth of the bubbles observed by a high-speed camera. The diameter and the growth speed of the bubbles can be estimated via frame-by-frame analysis. (e) 2D plots of the numerical simulation of the velocity of the flow around the microrotor in the $X-Y$ plane. The velocities are represented by a colored heat map from 0 μm/s (white) to 270 μm/s (deep blue), and the red arrows are velocity vectors. The flow field around the microrotor reaches the equilibrium state when the time reaches 2.8 s. (f) Simulation result showing that the rotation speed fits the experimental results.

of the microrotor [inset of Figure 1a(ii)], the Pt ions in the precursor are reduced to platinum nanoparticle clusters *in situ* in the laser spot (Note S2). After the two-step fabrication process, the sample is rinsed and H_2O_2 is dropped for actuation [Figure 1a(iii)]. Finally, the as-prepared microrotor enables steady rotation in a fuel liquid by bubble ejection force [Figure 1a(iv)].

To show the delicate and precise control of the SLMR, a "USTC" logo is patterned in the two-dimensional (2D) planar substrate (Figure S2). To obtain a sufficient amount of reduction of Pt and to minimize the thermal effect, we chose a laser power of 6 mW as a trade-off to realize SLMR and to match the power of DLW (Figure S3). The surface roughness of the Pt nanowire is ∼140 nm measured by an atomic force microscope (Figure S4). It is worth mentioning that SLMR shows good performance for the deposition of metal nanoparticles on glass, polymer surfaces, and other material surfaces (Figure S5). After DLW, the black area in Figure 1b indicates the selectively deposited catalytic Pt nanoparticles, where oxygen bubbles are ejected after the addition of the fuels. Eventually, the developed microrotor could rotate steadily at high speed (Figure 1b and Movie S2). The SEM and EDS images (Figure 1c) demonstrate the successful deposition of the Pt nanoparticle clusters into each cavity of the microrotor blades. Notably, Pt is deposited inside the cavity of the blades, rather than in the upper or lower surface of the blades, which can generate effective thrust power (Figure S6). In this way, the precise deposition control of ejection direction could be realized by SLMR. Finally, combining SLMR with DLW further enables both customization and array preparation of microrotors (Figure S7).

Mechanism and Simulation of Microrotor Rotation. As shown in Figure 2a, the microrotor generates reverse thrust, which drives the blades of the microrotor to move in a directional rotation. Figure 2b shows the frame in which a micromotor ejects bubbles captured by a high-speed camera. To better understand the process and mechanism of the rotation behavior of the microrotor, we analyze the force applied to the microrotor. The results in Figure 2c show that the main forces affecting the rotation are bubble growth force F_{bubble} and viscous force F_{drag}. They form a pair of driven moment M_{b} and viscous resistance moment M_{d} that synergistically affect the rotation speed of the microrotor. Among them, driven moment M_{b} can be expressed as

$$M_{\mathrm{b}} = 3C_s\pi\rho r^2\dot{r}^2 l_{\mathrm{b}} \cos\,\theta \tag{1}$$

where C_s is the growth coefficient of the bubble, ρ is the density of the solution, r is the radius of the bubble, $\dot{r}$ is the speed of bubble growth, l_{b} is the distance from the centroid to the point of force action, and θ is the angle between the driving force and the direction of rotation.

The expression of viscous resistance moment M_{d} is given below:

$$M_{\mathrm{d}} = \frac{0.308\pi\tau\rho_1 a^5\omega^2}{Re^{0.5}} \tag{2}$$

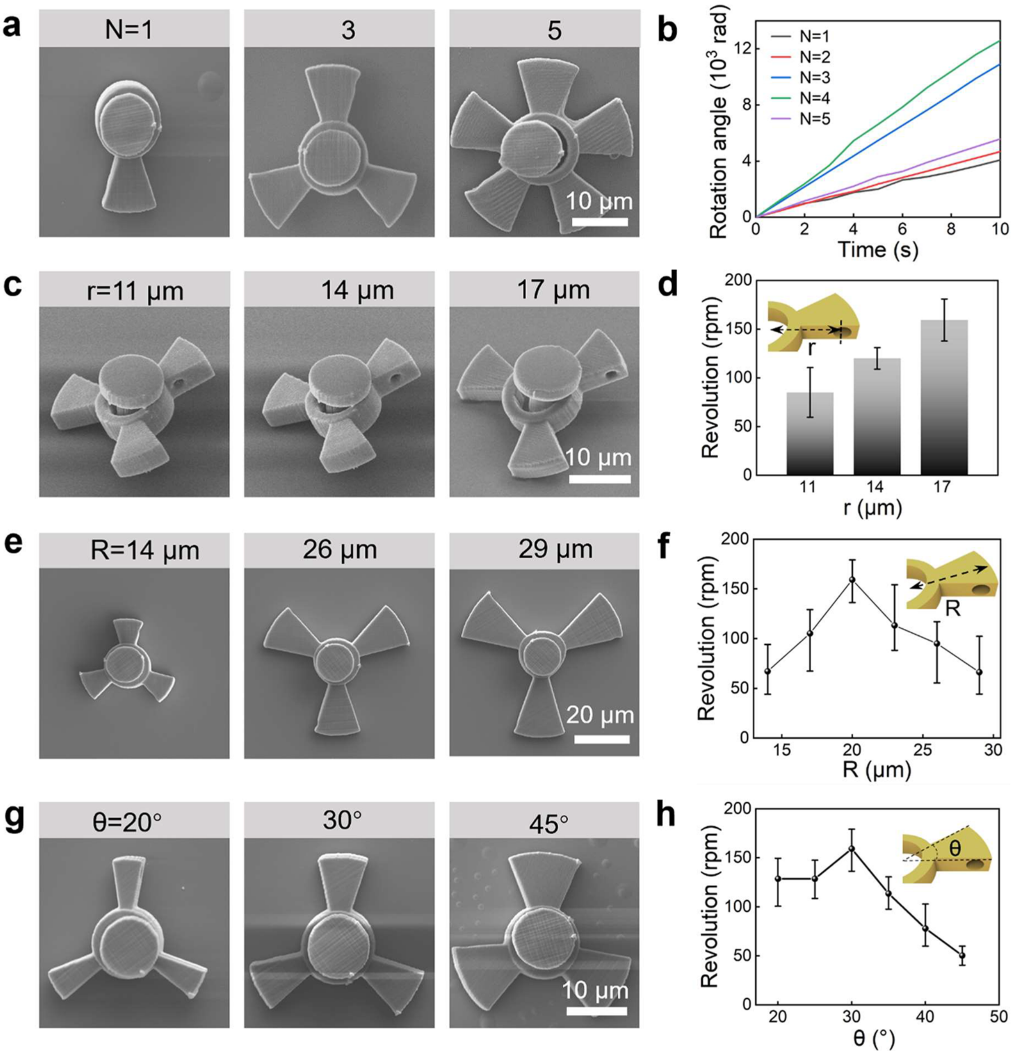

Figure 3. Controllable rotation speed of microrotors by shape design. (a) SEM image of a microrotor with different numbers of blades, where *N* represents the number of blades (from one to five). *N* values of one, three, and five blades are selected as representatives. (b) Time evolution of the cumulative rotation angle for the microrotors with different blades shown in Figure 3a. The smooth line indicates the steady rotation status of each rotor. (c) SEM image of blades with different cavity positions, where *r* represents the radius. The distance from the position of the center cavity to the geometric center of the microrotor ranges from 11 to 17 μm with an interval of 3 μm. (d) Diagram showing that the rotation speed increases with *r*. (e) SEM image of the three-blade microrotor with different radii, where *R* represents the radius of the microrotor. It denotes the distance from the geometric center of the microrotor to the edge of the blades. *R* values of 14, 26, and 29 μm are selected as representatives. (f) Trends of the revolution rate of the microrotors with the *R* of the blades. The error bar represents a unique standard deviation for that specific microrotor. (g) SEM image of the three-blade microrotor with different θ values. θ is the angle formed by the blade profile of the microrotor with the center of the microrotor. θ values of 20°, 30°, and 45° are selected as representatives. (h) Trends of the revolution rate of the rotors with the θ of the blades. The error bar represents a unique standard deviation for that specific microrotor.

where τ is a shape correction coefficient, ρ_l is the density of the medium liquid, a is the radius of the rotor, ω is the angular velocity of the rotor, and Re is the Reynolds number. The detailed theoretical analysis process can be found in Note S3.

In eq 1, the driven moment is related to the diameter and growth rate of the bubble. Under the 1000 frames per second high-speed camera, we captured the process of bubbles from nucleation in the holes of the blade to gradually expanding and ejecting; thus, the diameter and growth speed of the bubbles can be estimated on the basis of frame-by-frame analysis (Figure 2d and Figure S8).

To better evaluate the performance of the microrotor, we used the fluid−solid coupling simulation module[35] to further analyze the resistance and driving force of the system, and the fluid velocity in the vicinity of the microrotor is obtained (Figure 2e). Therefore, the simulation speed of the rotor is calculated by the correlation formula mentioned in Note S3. For a typical three-blade microrotor, the rotation speeds we measured are quite consistent with the simulation results (Figure 2f and Note S4).

Controllable Rotation Speed of Microrotors by Shape and Bubble Ejection Site Design. To adapt to a wider range of application scenarios, it is crucial to control the rotation speed of the microrotor. Thus, we investigated the relationship between the microrotor's shape and rotation speed by leveraging the flexibility of femtosecond laser processing (see Note S1 for a more detailed discussion of shape parameters). First, we design and prepare microrotors with different numbers of blades (N), from one to five (Figure 3a and Figure S9). While these prepared microrotors are

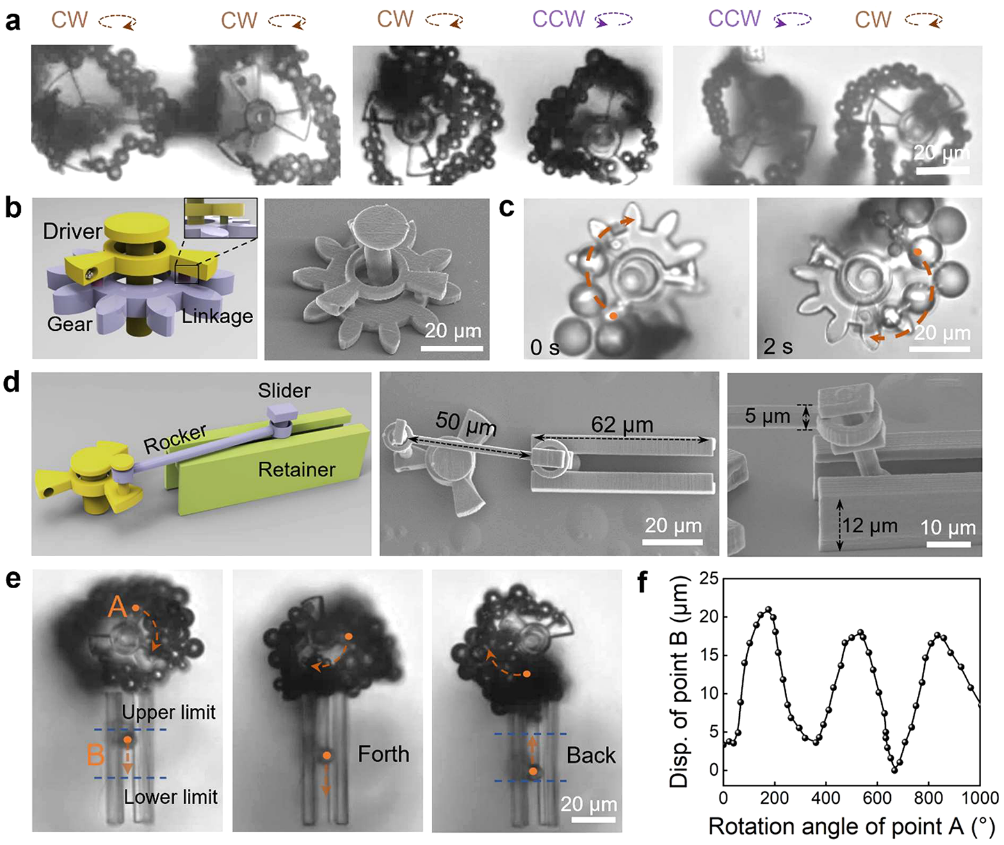

Figure 4. Microrotor for complex mechanical transmission. (a) Dual microrotor rotation with various modes realized by selective laser metal reduction, including dual microrotor rotation with the same clockwise (CW) directions, dual microrotor rotation with toward mode in CW and counterclockwise (CCW) directions independently, and dual microrotor rotation with the reverse mode in CCW and CW directions independently. (b) Schematic of a microcoupler system, in which the gear (blue) and the rotor (yellow) are linked by the three small short pillars (denoted in the inset) printed by DLW. The SEM image on the right shows the well-printed structure of the microcoupler. (c) Snapshots illustrate the microrotor rotation in the CW direction, which drives the gears rotary at the same pace. (d) Schematic of the crank slider system propelled by a microrotor. In the middle is the SEM image of the crank slider system (top view). On the right is a magnified partial SEM image of the interlock structures of the sliding block. The tilted sliding block indicates the dragging direction of the rotation rotor. (e) Snapshots show the trajectory of the crank slider system. It converts the rotational motion into the back-and-forth straight motion. (f) Rotation angle of point A of the microrotor as a function of the displacement of point B of the slider shown as a quasi-sine wave, indicating the relatively stable microsystem transmission process. Disp. stands for displacement.

immersed in an aqueous peroxide solution, they eject bubbles in a few seconds and gradually rotate to a steady state (Movie S3 and Figure S10). The time evolution of the cumulative rotation angle of the microrotor is shown in Figure 3b. The smooth and linear curves reveal the stable self-propulsion force generated by the microrotor. To better evaluate the performance of the microrotor under fuel supplementation, we measured the optimal speed of one to five microrotors in different concentrations of H_2O_2, the revolution speed of all kinds of microrotors is proportional to H_2O_2 concentration, while three- and four-blade microrotors are more sensitive at high fuel concentrations (Figure S11).

Next, we investigate the dependence of different cavity positions on rotation speed (Figure 3c). The cavity position radius (r) from the position of the center cavity on the side of the blades to the geometric center of the microrotor ranges from 11 to 17 μm, with the highest speed achieved by the 17 μm configuration (Figure 3d, Figure S12, and Movie S4). In addition, the torque of microrotors depends on their radius (R). Therefore, we investigate the influence of R on microrotor motion performance. With an increase in the side length of the blades from 6 to 21 μm with a length interval of 3 μm, while keeping the inner ring radius equal to 8 μm, R increases from 14 to 29 μm (Figure 3e and Figure S13). The microrotor rotation speed increases with R ranging from 14 to 20 μm and gradually decreases with R ranging from 20 to 29 μm (Figure 3f and Movie S5). In addition, similar behavior is observed by tuning the contour angle (θ) of the blades from 20° to 45° with a degree interval of 5°. As shown in Figure 3g and Figure S14, the increased value makes the rotor rotate faster in the range from 20° to 30°, and the rotor reaches the highest rotation speed of 162 rpm at a value of 30°. Then the rotation speed of the microrotor decreased linearly with a further increase in θ (Figure 3h and Movie S6).

Microrotor for Complex Mechanical Transmission. In recent years, micromotors with simple shapes like a microsphere or microtube have been widely reported[36,37] and found applications in medical treatment, environmental remediation, and biosensing. While the simple architectures of these micromotors exhibit reliable driving performance, the lack of designable 3D shapes largely increases the difficulty of system integration and functionality enhancement. To introduce additional functionalities for a microsystem, one feasible way is the integration of structural units or components. By taking

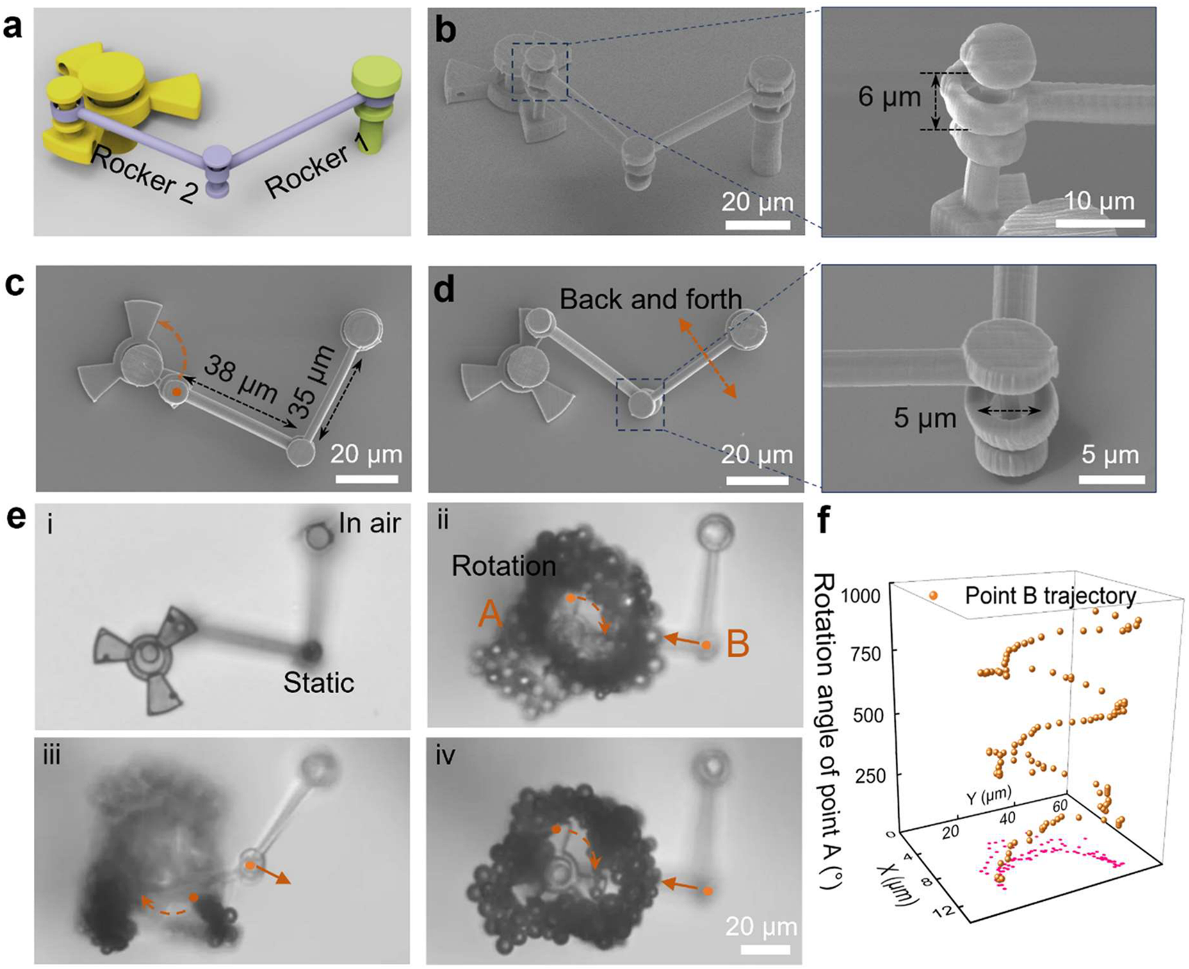

Figure 5. Crank rocker transmission system. (a) Schematic of a crank rocker system. (b) On the left is the SEM image showing the well-defined structure of the crank rocker system (45° top view). On the right is the magnified SEM image of the interlock structures of the crank rocker. (c) The SEM image shows the plan view of the crank rocker system. (d) On the left is the SEM image showing that after the microrotor in Figure 5c rotates through a certain angle, it drives the rocker to a new position. On the right is the magnified SEM image of the junction points of the crank rocker system. (e) Snapshots i−iv illustrate the microrotor rotation in the CW direction, which drives the rocking bar to sway at a regular pace, and it converts the rotational motion into sway motion. (f) Trajectory of the extension bar of the crank rocker system (point B), indicating a reliable transformation from rotation movement to sway movement.

advantage of the proposed processing strategy, we have demonstrated micromechanical systems based on a local-to-whole strategy that involves microrotors as power output components and complex multiple components.

Before performing micromechanical systems, we first demonstrate the ability to control the direction of microrotors. In Figure 4a, for a pair of microrotors, three rotation states are demonstrated to show the capability to individually control the rotation direction, including rotation in the identical direction, rotation toward each other, and rotation in the reverse direction (Movie S7 and Figure S15). Next, a series of experiments of the as-prepared microrotor, including the duration time, rotating cycle, rotation in colored liquids (Movie S8), and liquids containing magnetic particles, are conducted, demonstrating the robustness of the microrotor (Figures S16−S19).

In the following step, we demonstrate the fabrication of the structures expanded from a single rotor to a microsystem called a microcoupler. The schematic of a typical microcoupler system is demonstrated in Figure 4b, and it mainly comprises two parts, the passive gear (blue) and the driving rotor (yellow). The SEM images show the composition of the microgear, consisting of a three-blade microrotor and a 10-tooth microgear connected to the microrotor by three short pillars. The microrotor can drive other integrated components at the same pace due to strong thrust and load capacity (Movie S9, clip 1, and Figure 4c). On the basis of this concept, another microdevice like a dual-gear transmission can also be achieved (Movie S9, clip 2, and Figure S20).

Furthermore, more complex mechanical transmission systems are achieved. The crank slider system is a particular four-bar linkage configuration that could convert rotary motion into reciprocating motion and has wide application in industrial production. However, it is hard to conduct tasks on the microscale due to inherent size limitations. In our study, the micro-rocker system that can perform a rotary motion into back-and-forth linear motion is completed (Figure 4d). The morphology of the as-prepared micro-crank slider system is characterized by SEM in Figure 4d. The total length of the whole structure is ~120 μm, and the total width of the structures is <30 μm. The enlarged SEM image of the slider illustrates the details of the interlock connection of the movable rod and the sliding block (Figure S21). This interlocking junction is reliable, ensuring the stable and efficient operation of the system. The detailed operation process of the crank slider is shown in snapshots i−iii of Figure 4e from Movie S10. The movement of the slider from the upper to the lower limit is defined as the forward direction. As the crank rotates in the clockwise direction for the first 180°, it forces the connecting rod to drive slides forward; when the crank rotates the next 180°, the connecting rod pulls the slide back again to the upper limit. This process is repeated as the rotor spins without stopping (Figure S22). The quasi-sine wave line in Figure 4f illustrates the relationship between the rotation angle of the crank with the displacement of the slider.

Microrotor for a Crank Rocker Transmission System. In addition to the crank slider system, another four-bar linkage called the crank rocker system is designed (Figure 5a) and fabricated (Figure 5b). It is one of the most useful systems that can convert the rotary motion of the crank into a curved sway motion (Figure S23). The plan view of the crank rocker system is shown in Figure 5c. The interlocking structures with a clearance of 1.5 μm realized by DLW facilitate reliable power transmission (Figure 5d). In Figure 5e, snapshots i−iv from Movie S11 illustrate the operation of the crank rocker for one whole circle. When it is exposed to air, the crank remains static [Figure 5e(i)]. While a fuel solution is added, the rotor starts to rotate in the clockwise direction; in the first 180° of rotation, the force is transferred from the crank to rocker 1, which pulls rocker 2 toward the rotor [Figure 5e(ii)]. When rocker 2 reaches the upper limit [Figure 5e(iii)], it stops moving. Meanwhile, the rotor continues the next 180° rotation, which pushes the bar away from the rotor until a lower limit is reached [Figure 5e(iv)]. Total deviated angle θ is measured to be 40°. Figure 5f shows the trajectory of the rocker junction, indicating the reliable and smooth transmission of the prepared miniature crank rocker system. As a demonstration of a new concept, these regular rocking motions enable the opening and closing of microvalves, allowing potential applications, including flow control, transporting, and sorting of particles and cells.

Many useful types of mechanical systems have been reported over the years,[38−40] but the mechanical transmission systems in this work (illustrated in Figures 4 and 5) are active and self-propelled 3D mechanical architectures that are seldom realized. Our proposed approach reduces the number of tedious process steps and increases the spatial and geometric flexibility of the 3D free-standing micromechanical system. To the best of our knowledge, we built up the smallest crank slider and crank rocker system based on this approach. Although our current design has some limitations, e.g., both the position and the trajectory of the micromachines will be fixed once the fabrication is completed. In addition, the gaps and frictions between each component may cause delay or instability in transmission, but these drawbacks can be improved by the introduction of stimulus-responsive materials or rational predesign.[41−43] In addition, the current Pt catalyst can be replaced by other optional materials, including Au, Ag, Fe, and Ni for multifunction.[44,45] In particular, the addition of magnetic materials such as Fe, ferric oxide, and Ni facilitates a magnetic driving mechanism for biological applications.[46,47] Upon introduction of an external field or biocompatibility actuation, the rotation behavior of the microrotor and associated microsystems can be better controlled to achieve functions such as cell transport, mixing, and sorting.

In conclusion, a general strategy is proposed for constructing micromechanical systems with selective bubble ejection sites by incorporating laser-induced metallic selective reduction with femtosecond laser direct writing. Beyond the example of microrotors introduced here, the site-selected flexibility of Fs-DLW and SLMR can be applied to precisely modify other micromachines with sophisticated geometry, ranging from a single driving component to intricate 3D multicomponent architectures. We also experimentally and theoretically verify the effects of shape and bubble ejection sites on the performance of the microrotor, thereby optimizing the rotor speed to ∼160 rpm. Furthermore, the microrotor can be used as a stable power source for the transmission of various micromechanical systems. As a proof of concept, we design and demonstrate multicomponent mechanical systems, including microcoupling, a crank slider, and a crank rocker system.

■ ASSOCIATED CONTENT

SI Supporting Information

The Supporting Information is available free of charge at https://pubs.acs.org/doi/10.1021/acs.nanolett.4c00037.

Experimental details of the fabrication setup and methods; selection of the parameters of the microrotor; principles of photoreduction; numerical theory and simulation; contour graph of a microrotor; SEM image of patterned platinum nanoparticles; line widths of platinum nanoparticles and SZ2080; atomic force microscopy image of the Pt line width; optical images of different patterns; SEM image of a bubble ejection site; SEM image of a microrotor array; bubble ejection captured by a high-speed camera; optical image of different microrotors; data of microrotors with different numbers of blades, hydrogen peroxide concentrations, cavity locations, radii, and contour angles; SEM image of dual rotors; data of microrotors with times, cycles, and different liquid environments; and SEM images and data for different micromachine designs (PDF)

Demonstration of the hybrid fabrication methods of DLW combined with SLMR (Movie S1) (MP4)

Three-blade microrotor accelerating from a standstill to steady rotation in a short period of time (Movie S2) (MP4)

Rotation at different angular velocities of microrotors with different numbers of blades (Movie S3) (MP4)

Rotation at different angular velocities of microrotors with different cavity positions (Movie S4) (MP4)

Rotation at different angular velocities of microrotors with different microrotor radii (Movie S5) (MP4)

Rotation at different angular velocities of microrotors with different contour angles of blades (Movie S6) (MP4)

Dual microrotors that rotate independently in different modes (Movie S7) (MP4)

Three-blade microrotor's rotation without being affected by light in various colored solution environments (Movie S8) (MP4)

Microcoupling and microgear transmission (Movie S9) (MP4)

Crank slider system transmission (Movie S10) (MP4)

Crank rocker system transmission (Movie S11) (MP4)

AUTHOR INFORMATION

Corresponding Authors

Chen Xin − *CAS Key Laboratory of Mechanical Behavior and Design of Materials, Department of Precision Machinery and Precision Instrumentation, University of Science and Technology of China, Hefei, Anhui 230026, China; Department of Mechanical and Automation Engineering, The Chinese University of Hong Kong, Hong Kong 999077, China*; Email: xinc@ustc.edu.cn

Dong Wu − *CAS Key Laboratory of Mechanical Behavior and Design of Materials, Department of Precision Machinery and Precision Instrumentation, University of Science and Technology of China, Hefei, Anhui 230026, China*; orcid.org/0000-0003-0623-1515; Email: dongwu@ustc.edu.cn

Authors

Dawei Wang − *CAS Key Laboratory of Mechanical Behavior and Design of Materials, Department of Precision Machinery and Precision Instrumentation, University of Science and Technology of China, Hefei, Anhui 230026, China*

Liang Yang − *Suzhou Institute for Advanced Research, University of Science and Technology of China, Suzhou 215123, China*; orcid.org/0000-0001-6103-6451

Liu Wang − *CAS Key Laboratory of Mechanical Behavior and Design of Materials, Department of Modern Mechanics, University of Science and Technology of China, Hefei, Anhui 230026, China*; orcid.org/0000-0001-7014-9976

Bingrui Liu − *CAS Key Laboratory of Mechanical Behavior and Design of Materials, Department of Precision Machinery and Precision Instrumentation, University of Science and Technology of China, Hefei, Anhui 230026, China*; orcid.org/0000-0002-1245-0338

Hao Wu − *CAS Key Laboratory of Mechanical Behavior and Design of Materials, Department of Precision Machinery and Precision Instrumentation, University of Science and Technology of China, Hefei, Anhui 230026, China*

Chaowei Wang − *CAS Key Laboratory of Mechanical Behavior and Design of Materials, Department of Precision Machinery and Precision Instrumentation, University of Science and Technology of China, Hefei, Anhui 230026, China*

Deng Pan − *Information Materials and Intelligent Sensing Laboratory of Anhui Province, Anhui University, Hefei 230601, China*

Zhongguo Ren − *CAS Key Laboratory of Mechanical Behavior and Design of Materials, Department of Precision Machinery and Precision Instrumentation, University of Science and Technology of China, Hefei, Anhui 230026, China*

Yanlei Hu − *CAS Key Laboratory of Mechanical Behavior and Design of Materials, Department of Precision Machinery and Precision Instrumentation, University of Science and Technology of China, Hefei, Anhui 230026, China*; orcid.org/0000-0003-1964-0043

Jiawen Li − *CAS Key Laboratory of Mechanical Behavior and Design of Materials, Department of Precision Machinery and Precision Instrumentation, University of Science and Technology of China, Hefei, Anhui 230026, China*; orcid.org/0000-0003-3950-6212

Jiaru Chu − *CAS Key Laboratory of Mechanical Behavior and Design of Materials, Department of Precision Machinery and Precision Instrumentation, University of Science and Technology of China, Hefei, Anhui 230026, China*; orcid.org/0000-0001-6472-8103

Complete contact information is available at: https://pubs.acs.org/10.1021/acs.nanolett.4c00037

Author Contributions

C.X. and D. Wu conceived the idea and organized the project. D. Wang, L.Y., Z.R., D.P., and B.L. performed the experiments under the guidance of Y.H., J.L., J.C., and D. Wu. All authors contributed to the discussion of the experimental results. D. Wu supervised the project. D. Wang and C.X. wrote the manuscript with contributions from all co-authors.

Funding

This work was supported by the National Natural Science Foundation of China (61927814, 62325507, 52122511, 52375582, 62205236, 62005262, 62275242, and 62305321), the National Key Research and Development Program of China (2021YFF0502700), the Major Scientific and Technological Projects in Anhui Province (202203a05020014), the USTC Research Funds of the Double First-Class Initiative (YD2340002009), and the CAS Project for Young Scientists in Basic Research (YSBR-049).

Notes

The authors declare no competing financial interest.

ACKNOWLEDGMENTS

The authors acknowledge the Experimental Center of Engineering and Material Sciences at the University of Science and Technology of China (USTC) for the fabrication and measuring of samples. This work was partly carried out at the USTC Center for Micro and Nanoscale Research and Fabrication.

REFERENCES

(1) Ussia, M.; Pumera, M. Towards Micromachine Intelligence: Potential of Polymers. *Chem. Soc. Rev.* **2022**, *51* (5), 1558−1572.

(2) Li, J.; Esteban-Fernández de Avila, B.; Gao, W.; Zhang, L.; Wang, J. Micro/Nanorobots for Biomedicine: Delivery, Surgery, Sensing, and Detoxification. *Science Robotics* **2017**, *2* (4), No. eaam6431.

(3) Kim, K.; Guo, J.; Liang, Z. X.; Zhu, F. Q.; Fan, D. L. Man-made Rotary Nanomotors: A Review of Recent Developments. *Nanoscale* **2016**, *8* (20), 10471−90.

(4) Xia, H.; Wang, J.; Tian, Y.; Chen, Q.-D.; Du, X.-B.; Zhang, Y.-L.; He, Y.; Sun, H.-B. Ferrofluids for Fabrication of Remotely Controllable Micro-Nanomachines by Two-Photon Polymerization. *Adv. Mater.* **2010**, *22* (29), 3204−3207.

(5) Matsunaga, D.; Hamilton, J. K.; Meng, F.; Bukin, N.; Martin, E. L.; Ogrin, F. Y.; Yeomans, J. M.; Golestanian, R. Controlling Collective Rotational Patterns of Magnetic Rotors. *Nat. Commun.* **2019**, *10* (1), 4696.

(6) Zhang, S.; Elsayed, M.; Peng, R.; Chen, Y.; Zhang, Y.; Peng, J.; Li, W.; Chamberlain, M. D.; Nikitina, A.; Yu, S.; Liu, X.; Neale, S. L.; Wheeler, A. R. Reconfigurable Multi-Component Micromachines Driven by Optoelectronic Tweezers. *Nat. Commun.* **2021**, *12* (1), 5349.

(7) Loget, G.; Kuhn, A. Electric Field-Induced Chemical Locomotion of Conducting Objects. *Nat. Commun.* **2011**, *2*, 535.

(8) Bianchi, S.; Vizsnyiczai, G.; Ferretti, S.; Maggi, C.; Di Leonardo, R. An Optical Reaction Micro-Turbine. *Nat. Commun.* **2018**, *9* (1), 4476.

(9) Wu, X.; Ehehalt, R.; Razinskas, G.; Feichtner, T.; Qin, J.; Hecht, B. Light-Driven Microdrones. *Nat. Nanotechnol.* **2022**, *17* (5), 477−484.

(10) Liu, M.; Zentgraf, T.; Liu, Y.; Bartal, G.; Zhang, X. Light-Driven Nanoscale Plasmonic Motors. *Nat. Nanotechnol.* **2010**, *5* (8), 570−573.

(11) Zhou, Y.; Wang, H.; Ma, Z.; Yang, J. K. W.; Ai, Y. Acoustic Vibration-Induced Actuation of Multiple Microrotors in Microfluidics. *Adv. Mater. Technol.* **2020**, *5* (9), 2000323.

(12) Bertin, N.; Spelman, T. A.; Stephan, O.; Gredy, L.; Bouriau, M.; Lauga, E.; Marmottant, P. Propulsion of Bubble-Based Acoustic Microswimmers. *Phys. Rev. Appl.* **2015**, *4* (6), 064012.

(13) Aghakhani, A.; Pena-Francesch, A.; Bozuyuk, U.; Cetin, H.; Wrede, P.; Sitti, M. High Shear Rate Propulsion of Acoustic Microrobots in Complex Biological Fluids. *Sci. Adv.* **2022**, *8* (10), No. eabm5126.

(14) Butaite, U. G.; Gibson, G. M.; Ho, Y. D.; Taverne, M.; Taylor, J. M.; Phillips, D. B. Indirect Optical Trapping Using Light-Driven Micro-Rotors for Reconfigurable Hydrodynamic Manipulation. *Nat. Commun.* **2019**, *10* (1), 1215.

(15) Sitti, M.; Wiersma, D. S. Pros and Cons: Magnetic versus Optical Microrobots. *Adv. Mater.* **2020**, *32* (20), No. e1906766.

(16) Xin, C.; Yang, L.; Li, J.; Hu, Y.; Qian, D.; Fan, S.; Hu, K.; Cai, Z.; Wu, H.; Wang, D.; Wu, D.; Chu, J. Conical Hollow Microhelices with Superior Swimming Capabilities for Targeted Cargo Delivery. *Adv. Mater.* **2019**, *31* (25), No. e1808226.

(17) Maggi, C.; Saglimbeni, F.; Dipalo, M.; De Angelis, F.; Di Leonardo, R. Micromotors with Asymmetric Shape that Efficiently Convert Light into Work by Thermocapillary Effects. *Nat. Commun.* **2015**, *6* (1), 7855.

(18) Baker, R. D.; Montenegro-Johnson, T.; Sediako, A. D.; Thomson, M. J.; Sen, A.; Lauga, E.; Aranson, I. S. Shape-Programmed 3D Printed Swimming Microtori for the Transport of Passive and Active Agents. *Nat. Commun.* **2019**, *10* (1), 4932.

(19) Mei, Y.; Solovev, A. A.; Sanchez, S.; Schmidt, O. G. Rolled-up Nanotech on Polymers: From Basic Perception to Self-Propelled Catalytic Microengines. Chem. *Soc. Rev.* **2011**, *40* (5), 2109−2119.

(20) Solovev, A. A.; Mei, Y.; Bermudez Urena, E.; Huang, G.; Schmidt, O. G. Catalytic Microtubular Jet Engines Self-Propelled by Accumulated Gas Bubbles. *Small* **2009**, *5* (14), 1688−1692.

(21) Wilson, D. A.; Nolte, R. J.; van Hest, J. C. Autonomous Movement of Platinum-Loaded Stomatocytes. *Nat. Chem.* **2012**, *4* (4), 268−274.

(22) Brooks, A. M.; Tasinkevych, M.; Sabrina, S.; Velegol, D.; Sen, A.; Bishop, K. J. M. Shape-Directed Rotation of Homogeneous Micromotors via Catalytic Self-Electrophoresis. *Nat. Commun.* **2019**, *10* (1), 495.

(23) Maggi, C.; Simmchen, J.; Saglimbeni, F.; Katuri, J.; Dipalo, M.; De Angelis, F.; Sanchez, S.; Di Leonardo, R. Self-Assembly of Micromachining Systems Powered by Janus Micromotors. *Small* **2016**, *12* (4), 446−451.

(24) Xu, C.; Wang, S.; Wang, H.; Liu, K.; Zhang, S.; Chen, B.; Liu, H.; Tong, F.; Peng, F.; Tu, Y.; Li, Y. Magnesium-Based Micromotors as Hydrogen Generators for Precise Rheumatoid Arthritis Therapy. *Nano Lett.* **2021**, *21* (5), 1982−1991.

(25) Chen, C.; Karshalev, E.; Guan, J.; Wang, J. Magnesium-Based Micromotors: Water-Powered Propulsion, Multifunctionality, and Biomedical and Environmental Applications. *Small* **2018**, *14* (23), 1704252.

(26) Mei, Y.; Huang, G.; Solovev, A. A.; Ureña, E. B.; Mönch, I.; Ding, F.; Reindl, T.; Fu, R. K. Y.; Chu, P. K.; Schmidt, O. G. Versatile Approach for Integrative and Functionalized Tubes by Strain Engineering of Nanomembranes on Polymers. *Adv. Mater.* **2008**, *20* (21), 4085−4090.

(27) Doherty, R. P.; Varkevisser, T.; Teunisse, M.; Hoecht, J.; Ketzetzi, S.; Ouhajji, S.; Kraft, D. J. Catalytically Propelled 3D Printed Colloidal Microswimmers. *Soft Matter* **2020**, *16* (46), 10463−10469.

(28) Catchmark, J. M.; Subramanian, S.; Sen, A. Directed Rotational Motion of Microscale Objects Using Interfacial Tension Gradients Continually Generated via Catalytic Reactions. *Small* **2005**, *1* (2), 202−206.

(29) Ceylan, H.; Yasa, I. C.; Sitti, M. 3D Chemical Patterning of Micromaterials for Encoded Functionality. *Adv. Mater.* **2017**, *29* (9), 1605072.

(30) Wu, Z.; Li, L.; Yang, Y.; Hu, P.; Li, Y.; Yang, S.-Y.; Wang, L. V.; Gao, W. A Microrobotic System Guided by Photoacoustic Computed Tomography for Targeted Navigation in Intestines In Vivo. *Science Robotics* **2019**, *4* (32), No. eaax0613.

(31) Solovev, A. A.; Sanchez, S.; Pumera, M.; Mei, Y. F.; Schmidt, O. G. Magnetic Control of Tubular Catalytic Microbots for the Transport, Assembly, and Delivery of Micro-objects. *Adv. Funct. Mater.* **2010**, *20* (15), 2430−2435.

(32) Lao, Z.; Xia, N.; Wang, S.; Xu, T.; Wu, X.; Zhang, L. Tethered and Untethered 3D Microactuators Fabricated by Two-Photon Polymerization: A Review. *Micromachines* **2021**, *12* (4), 465.

(33) Chen, Y. S.; Tal, A.; Torrance, D. B.; Kuebler, S. M. Fabrication and Characterization of Three-Dimensional Silver-Coated Polymeric Microstructures. *Adv. Funct. Mater.* **2006**, *16* (13), 1739−1744.

(34) Xu, J.; Li, X.; Zhong, Y.; Qi, J.; Wang, Z.; Chai, Z.; Li, W.; Jing, C.; Cheng, Y. Glass-Channel Molding Assisted 3D Printing of Metallic Microstructures Enabled by Femtosecond Laser Internal Processing and Microfluidic Electroless Plating. *Adv. Mater. Technol.* **2018**, *3* (12), 1800372.

(35) Wu, H.; Chen, Y.; Xu, W.; Xin, C.; Wu, T.; Feng, W.; Yu, H.; Chen, C.; Jiang, S.; Zhang, Y.; et al. High-performance Marangoni Hydrogel Rotors with Asymmetric Porosity and Drag Reduction Profile. *Nat. Commun.* **2023**, *14* (1), 20.

(36) Xin, C.; Jin, D.; Hu, Y.; Yang, L.; Li, R.; Wang, L.; Ren, Z.; Wang, D.; Ji, S.; Hu, K.; Pan, D.; Wu, H.; Zhu, W.; Shen, Z.; Wang, Y.; Li, J.; Zhang, L.; Wu, D.; Chu, J. Environmentally Adaptive Shape-Morphing Microrobots for Localized Cancer Cell Treatment. *ACS. Nano.* **2021**, *15* (11), 18048−18059.

(37) Xu, B.; Zhang, B.; Wang, L.; Huang, G.; Mei, Y. Tubular Micro/Nanomachines: From the Basics to Recent Advances. *Adv. Funct. Mater.* **2018**, *28* (25), 1705872.

(38) Hu, X.; Yasa, I. C.; Ren, Z.; Goudu, S. R.; Ceylan, H.; Hu, W.; Sitti, M. Magnetic Soft Micromachines Made of Linked Microactuator Networks. *Sci. Adv.* **2021**, *7* (23), No. eabe8436.

(39) Kong, L.; Ambrosi, A.; Nasir, M. Z. M.; Guan, J.; Pumera, M. Self-Propelled 3D-Printed "Aircraft Carrier" of Light-Powered Smart Micromachines for Large-Volume Nitroaromatic Explosives Removal. *Adv. Funct. Mater.* **2019**, *29* (39), 1903872.

(40) Dong, Y.; Wang, L.; Zhang, Z.; Ji, F.; Chan, T. K.; Yang, H.; Chan, C. P.; Yang, Z.; Chen, Z.; Chang, W. T.; et al. Endoscope-Assisted Magnetic Helical Micromachine Delivery for Biofilm Eradication in Tympanostomy Tube. *Sci. Adv.* **2022**, *8* (40), No. eabq8573.

(41) Ceylan, H.; Dogan, N. O.; Yasa, I. C.; Musaoglu, M. N.; Kulali, Z. U.; Sitti, M. 3D Printed Personalized Magnetic Micromachines from Patient Blood−Derived Biomaterials. *Sci. Adv.* **2021**, *7* (36), No. eabh0273.

(42) Jeon, S.; Kim, S.; Ha, S.; Lee, S.; Kim, E.; Kim, S. Y.; Park, S. H.; Jeon, J. H.; Kim, S. W.; Moon, C.; et al. Magnetically Actuated Microrobots as a Platform for Stem Cell Transplantation. *Science Robotics* **2019**, *4* (30), No. eaav4317.

(43) Xin, C.; Ren, Z.; Zhang, L.; Yang, L.; Wang, D.; Hu, Y.; Li, J.; Chu, J.; Zhang, L.; Wu, D. Light-Triggered Multi-Joint Microactuator Fabricated by Two-in-One Femtosecond Laser Writing. *Nat. Commun.* **2023**, *14* (1), 4273.

(44) Chen, Y.; Hung, S. F.; Lo, W. K.; Chen, Y.; Shen, Y.; Kafenda, K.; Su, J.; Xia, K.; Yang, S. A Universal Method for Depositing Patterned Materials In Situ. *Nat. Commun.* **2020**, *11* (1), 5334.

(45) Li, D.; Liu, C.; Yang, Y.; Wang, L.; Shen, Y. Micro-Rocket Robot with All-Optic Actuating and Tracking in Blood. *Light: Sci. Appl.* **2020**, *9* (1), 84.

(46) Wang, H.; Xu, B. B.; Zhang, Y. L.; Kollipara, P. S.; Liu, S.; Lin, L.; Chen, Q. D.; Zheng, Y.; Sun, H. B. Light-Driven Magnetic Encoding for Hybrid Magnetic Micromachines. *Nano Lett.* **2021**, *21* (4), 1628−1635.

(47) Zarzar, L. D.; Swartzentruber, B.; Donovan, B. F.; Hopkins, P. E.; Kaehr, B. Using Laser-Induced Thermal Voxels to Pattern Diverse Materials at the Solid−Liquid Interface. *ACS Appl. Mater. Interfaces.* **2016**, *8* (33), 21134−21139.

https://doi.org/10.1021/acs.nanolett.4c00037